ADVANCED ENERGY MATERIALS

Supporting Information

for *Adv. Energy Mater.,* DOI: 10.1002/aenm.201401082

Design Principles for Metal Oxide Redox Materials for Solar-Driven Isothermal Fuel Production

Ronald Michalsky, Venkatesh Botu, Cory M. Hargus, Andrew A. Peterson, and Aldo Steinfeld*

Supporting Information

Design Principles for Metal Oxide Redox Materials for Solar-Driven Isothermal Fuel Production

Ronald Michalsky[*], *Venkatesh Botu, Cory M. Hargus, Andrew A. Peterson, Aldo Steinfeld*

1. Computational details

1.1. Thermodynamic equilibrium calculations

For computing Figure 1, the free energies of forming Ag_2O and Au_2O_3 at 1027°C and Mn_3O_4, MoO_3, RuO_2, SnO_2 and SnO at 1727°C were extrapolated linearly from the available literature data (taking the available data within a range of 300°C at the highest temperatures, yielding $R^2 > 0.996$).[1]

To quantify the correlation shown with Figure 3, we approximated the bulk-formation energies for BSCF and LSCF (both with oxygen vacancies formed at the Co atoms), LSM, and YSZ with those of Co_3O_4 (with a formal oxidation state of 2.27 *vs*. approximately 4 in BSCF and 3 in LSCF), Mn_2O_3 (with a formal oxidation state of 3.33 *vs*. about 3 in LSM), and ZrO_2 respectively, *i.e.*, with the bulk-formation energies of binary metal oxides in a relatively similar oxidation state.

1.2. Electronic structure calculations

To assess the possibility that the binding of CO at the metal oxide surface limits the solar-driven isothermal reduction of CO_2, the free energy of the CO adsorption, $\Delta G_B[CO]$, was calculated via:

$$\Delta G_B[CO] = G_{surf+CO} - (G_{surf} + G_{CO}^r) \quad \text{(S1)}$$

where $G_{surf+CO}$, G_{surf} and G_{CO}^r are the free energies of the surface and CO adsorbed at a metal-top site, the surface without the adsorbate and the reference energy of the CO adsorbate, *i.e.*, CO in the gas phase respectively.

1.3. Oxygen self-diffusion constants

We note the experimental value of the shown self-diffusion constant for CeO_2 includes values for $Ce_{0.9}Gd_{0.1}O_{2-\delta}$[2] and $CeO_{1.95}$[3] and the computed YSZ structure contains 25 mol% Y (metal basis) relative to 10-20 mol% for the experimental values.[2],[4],[5],[6],[7] Furthermore, for comparability, the experimental values for Ag_2O are the values of oxygen diffusing in metallic silver[8],[9],[10] and the value for Cu_2O is extrapolated for oxygen-vacancy conduction in Cu_2O (rather than Cu vacancies diffusing in $Cu_{2-\delta}O$).[11]

1.4. Reaction rate constants

The turnover frequency of a unimolecular oxygen-vacancy conduction that is assumed to limit an isothermal solar-driven H_2O splitting process liberating H_2 and filling oxygen vacancies at a metal oxide surface, k_{H2} in molecules H_2 site^{-1} s^{-1}, can be estimated from the free energy of the transition state:

$$k_{\mathrm{H_2}} = \frac{\mathrm{k_B}T}{\mathrm{h}} \exp\left\{\frac{-\Delta G_{\mathrm{TS}}[\mathrm{O}]}{\mathrm{k_B}T}\right\} \quad \text{(S2)}$$

where k_B is the Boltzmann constant in eV K^{-1}, T is the absolute temperature in K^{-1}, and h is the Planck constant in eV × s. Taking the approximate threshold of the transition state energy for oxygen conduction in metal oxides with a relatively low endergonic diffusion path (see Section 2.3), the peak H_2 formation rate, r_{H2}, can be estimated with:

$$r_{\mathrm{H_2}} = \frac{k_{\mathrm{H_2}} A_{\mathrm{BET}}}{\mathrm{N_A} A_{\mathrm{surface}}} p_{\mathrm{H_2O}} \quad \text{(S3)}$$

where N_A is Avogadro's number in molecules mol^{-1}, A_{BET} is the specific surface area of the redox material in m^2 g^{-1} (taken as 1.05 m^2 g^{-1} for a hercynite redox material),[12] $A_{surface}$ is the specific area of a reaction site in m^2 site^{-1} (taken as 30.24 Å site^{-1} for the $La_{0.5}Sr_{0.5}Co_{0.5}Fe_{0.5}O_3(010)$ surface model), and p_{H2O} is the partial pressure of H_2O during the oxidation (taken as 0.506 bar H_2O, relative to a total pressure of 1 bar).[12]

2. Supporting results and discussion

2.1. Surface energies

Table S1A: Metal oxide surface energies, E_s

r-TiO_2		Ti_2O_3		$Ba_{0.5}Sr_{0.5}Co_{0.5}Fe_{0.5}$		$La_{0.5}Sr_{0.5}Co_{0.5}Fe_{0.5}$	
Surface	**E_s/ J m^{-2}**	**Surface**	**E_s/ J m^{-2}**	**Surface**	**E_s/ J m^{-2}**	**Surface**	**E_s/ J m^{-2}**
mt(001)	1.62	mt(001)	1.70	FeO_2-SrO(001)	0.65	FeO_2-SrO(001)	a
Ot(010)	5.37	Ot(001)	2.17	BaO-CoO_2(001)	0.64	LaO-CoO_2(001)	0.93
Mt(010)	5.10	Mt(001)	3.79	SrO-CoO_2(001)	0.78	SrO-CoO_2(001)	0.70
mt(011)	1.14	mt(010)	1.41	FeO_2-BaO(001)	0.83	FeO_2-LaO(001)	0.80
Mt(011)	5.12	mt(011)	1.47	CoO_2-BaO(001)	0.77	CoO_2-LaO(001)	0.79
Ot(011)	5.35	Ot(011)	1.60	SrOFeO_2(001)	0.67	SrO-FeO_2(001)	0.70
Ot(110)	3.51	Mt(011)	1.49	BaO-FeO_2(001) [b]	0.56	LaO-FeO_2(001)	1.17
Mt(110)	3.22	mt1(101)	1.22	CoO_2-SrO(001)	0.61	CoO_2-SrO(001)	1.55
mt(110)	**0.73**	Mt1(101)	1.43	$CoFeO_4$(010)	0.77	$CoFeO_4$(010)	1.02
mt1(111)	2.33	Ot2(101)	1.62	**$BaSrO_2$(010)**	**0.63**	**$LaSrO_2$(010)**	**0.63**
mt2(111)	1.66	mt2(101)	1.64	SrO-FeO_2(011)	0.99	SrO-FeO_2(011)	1.08
mt3(111)	2.26	Ot1(101)	1.89	CoO_2-BaO(011)	1.06	CoO_2-LaO(011)	1.14
mt4(111)	2.65	Mt2(101)	1.64	FeO_2-BaO(011)	1.10	FeO_2-LaO(011)	1.18
		Ot1(110)	2.26	SrO-CoO_2(011)	1.00	SrO-CoO_2(011)	1.19
		mt1(110)	**0.94**	BaO-CoO_2(011)	0.97	LaO-CoO_2(011)	1.44
		Mt1(110)	1.37	FeO_2-SrO(011)	1.01	FeO_2-SrO(011)	1.56
		mt1(111)	0.99	CoO_2-SrO(011)	0.96	CoO_2-SrO(011)	1.45
		mt2(111)	1.18	BaOFeO_2(011)	0.96	LaO-FeO_2(011)	1.32
		mt3(111)	1.04	BaSrCoFeO_2(110)	a	LaSrCoFeO_2(110)	1.64
		mt4(111)	1.00	BaSrCoFeO_6(110)	1.28	LaSrCoFeO_6(110)	1.61
		mt5(111)	1.07	CoBaO(111)	1.07	CoLaO(111)	1.40
		mt6(111)	1.06	SrFeO(111)	1.06	SrFeO(111)	1.38
				BaFeO(111)	1.28	LaFeO(111)	1.23
				CoSrO(111)	1.11	CoSrO(111)	1.27
				FeSrO(111)	1.20	FeSrO(111)	1.45
				BaCoO(111)	1.07	LaCoO(111)	1.31
				SrCoO(111)	1.09	SrCoO(111)	1.46
				FeBaO(111)	1.21	FeLaO(111)	1.52

The surface indicates the surface termination followed by the crystal facet (mt*i*: mixed metal/oxygen-terminated with *i* being a running index, Mt*i*: metal-terminated, Ot*i*: oxygen-terminated, chemical species such as '$CoFeO_4$' indicate the composition of the terminating surface layer, two chemical species such as 'FeO_2-SrO' indicate the compositions of the surface and subsurface layer respectively); a) not converged; not chosen in this work to directly compare $BaSrO_2$(010)BSCF to $LaSrO_2$(010)LSCF; the selected low-energy surfaces are marked in bold and gray.

Table S1B: Metal oxide surface energies, E_s

$La_{0.67}Sr_{0.33}O_3$		w-ZnO		c-YSZ ($Y_2Zr_6O_{15}$)		MoO_3	
Surface	**E_s/ J m^{-2}**	**Surface**	**E_s/ J m^{-2}**	**Surface**	**E_s/ J m^{-2}**	**Surface**	**E_s/ J m^{-2}**
$SrLaMn_2O_6$(001)	a	Ot(001)	4.77	OtVL4(001)	5.05	Ot1(001)	1.78
$SrLaMnO_3$(001)	0.73	Mt(001)	4.88	MtVL3(001)	5.52	Ot2(001)	2.02
$La_2Mn_2O_6$(001)	**0.71**	mt1(001)	1.56	OtVL3(001)	4.18	mt(001)	2.41
La_2MnO_3(001)	a	mt2(001)	1.46	MtVL2(001)	5.49	Ot3(001)	2.51
$LaSrMn_2O_6$(001)	1.13	mt1(010)	2.36	OtVL2(001)	3.71	Ot4(001)	1.33
$LaSrMnO_3$(001)	1.11	**mt2(010)**	**0.87**	MtVL1(001)	6.84	mt(010) [b]	0.77
MnO_2(010)	1.08	mt(100)	0.89	OtVL1(001)	3.35	mt(100) [c]	0.05
La_2SrO_3(010)	1.04	Mt1(011)	2.98	MtVL4(001)	4.22	Ot1(100)	3.95
La_2MnO_4(011)	1.20	Ot1(011)	1.68	OtVL1(010)	3.71	Ot2(100) [c]	-0.13
$SrLaMnO_2$(011)	1.28	Mt2(011)	1.77	MtVL2(010)	3.85	Mt1(100)	3.30
La_2MnO_2(011)	1.42	Ot2(011)	1.73	OtVL2(010)	4.22	Ot3(100)	4.69
$SrLaMnO_4$(011)	1.38	mt1(101)	1.83	MtVL1(010)	4.45	Mt2(100)	7.87
$LaSrMnO_4$(011)	1.34	mt2(101)	1.81	mYZrOtVL4(011)	2.55	**mt1(011)**	**0.73**
$LaSrMnO_2$(011)	1.40	Ot(101)	2.50	OZrtVL1(011)	2.78	mt2(011)	1.75
$La_2SrMn_3O_6$(110)	1.03	Mt(101)	2.62	mZrOtVL3(011)	3.05	mt1(101)	1.32
$La_2SrMn_3O_3$(110)	1.97	mt1(110)	0.89	OYZrtVL2(011)	3.29	Ot(101)	1.44
$La_2SrMn_3O_9$(110)	1.66	mt2(110)	2.36	mZrOtVL2(011)	3.07	mt2(101)	1.08
La_2MnO_4(111)	1.46	Ot1(111)	2.21	OYZrtVL3(011)	3.13	mt3(101)	1.07
$LaSrMn_2O_6$(111)	1.63	Mt1(111)	2.35	mYZrOtVL1(011)	1.93	mt1(110)	0.75
$LaSrMnO_4$(111)	1.51	mt1(111)	1.67	OZrtVL4(011)	1.98	mt2(110)	1.37
$SrLaMn_2O_6$(111)	1.57	Ot2(111)	1.56	**mZrOtVL2(110)**	**1.11**	mt1(111)	1.07
$SrLaMnO_4$(111)	1.54	Mt2(111)	3.78	mYZrOtVL1(110)	1.21	Mt1(111)	1.30
$La_2Mn_2O_6$(111)	1.70	Ot3(111)	3.26	OYZrtVS4(111)	1.86	Ot1(111)	1.95
		mt2(111)	1.44	mYZrOtSL2(111)	1.93	Mt2(111)	1.78
		mt3(111)	1.58	OYZrtVS3(111)	1.67	Ot2(111)	1.57
				mYZrOtVS3(111)	1.84	mt2(111)	1.57
				OYZrtVS2(111)	2.03	mt3(111)	1.93
				mYZrOtVS4(111)	1.93		
				OYZrtVS1(111)	2.31		
				mYZrOtVS1(111)	2.30		

The surface indicates the surface termination followed by the crystal facet (mt*i*: mixed metal/oxygen-terminated with *i* being a running index, Mt*i*: metal-terminated, Ot*i*: oxygen-terminated, chemical species such as '$SrLaMn_2O_6$' indicate the composition of the terminating surface layer, for c-YSZ surface species are given in addition to the mt, Mt, and Ot notation for clarity and VL*j* marks the layer of the bulk model that contains the natural oxygen vacancy); a) not converged; b) the most commonly studied MoO_3 surface that is only by about 43.5 mJ m^{-2} less stable than the more complex surface chosen in this work; c) unstable due to separation of the surface layers; the selected low-energy surfaces are marked in bold and gray.

Table S1C: Metal oxide surface energies, E_s

Cu_2O		c-ZrO_2		Ag_2O		CeO_2	
Surface	**E_s/ J m^{-2}**	**Surface**	**E_s/ J m^{-2}**	**Surface**	**E_s/ J m^{-2}**	**Surface**	**E_s/ J m^{-2}**
Mt(001)	1.17	Ot(001)	5.51	Mt(001)	0.83	Ot(001)	6.86
mt(001)	1.37	Mt(001)	5.45	mt(001)	0.95	Mt(001)	3.82
Mt(011)	0.92	**mt(011)**	**1.36**	Mt(011)	0.62	mt(011)	5.40
mt(011)	0.97	mt(111)	6.64	mt(011)	0.67	mt(111)	4.24
mt(111)	**0.62**	Mt(111)	6.64	**mt(111)**	**0.39**	Mt(111)	4.78
Ot(111)	1.52	Ot(111)	6.55	Ot(111)	1.07	**Ot(111)**	**1.39**
Mt(111)	1.40			Mt(111)	0.97		

The surface indicates the surface termination followed by the crystal facet (mt*i*: mixed metal/oxygen-terminated with *i* being a running index, Mt*i*: metal-terminated, Ot*i*: oxygen-terminated); the selected low-energy surfaces are marked in bold and gray.

2.2. CO chemisorption

Table S2: Free energies of CO adsorbed at metal oxide surfaces

surface	E_B[CO] / eV	top site	d_{M-C} / Å
TiO_2(110)	0.44	Ti	2.67
Ti_2O_3(110)	0.07	Ti	2.17
LSM(001)	0.37	Mn	2.26
BSCF(010)	0.32	Sr	3.27
LSCF(010)	0.30	Sr	3.16
Cu_2O(111)	-0.96	Cu	1.82
ZnO(010)	0.34	Zn	2.27
ZrO_2(011)	0.14	Zr	2.64
YSZ(110)	0.20	Zr	2.67
MoO_3(011)	0.39	a	-
Ag_2O(111)	-0.44	Ag	1.99
CeO_2(111)	0.27	Ce	-

a) not adsorbed

2.3. Electronic structure

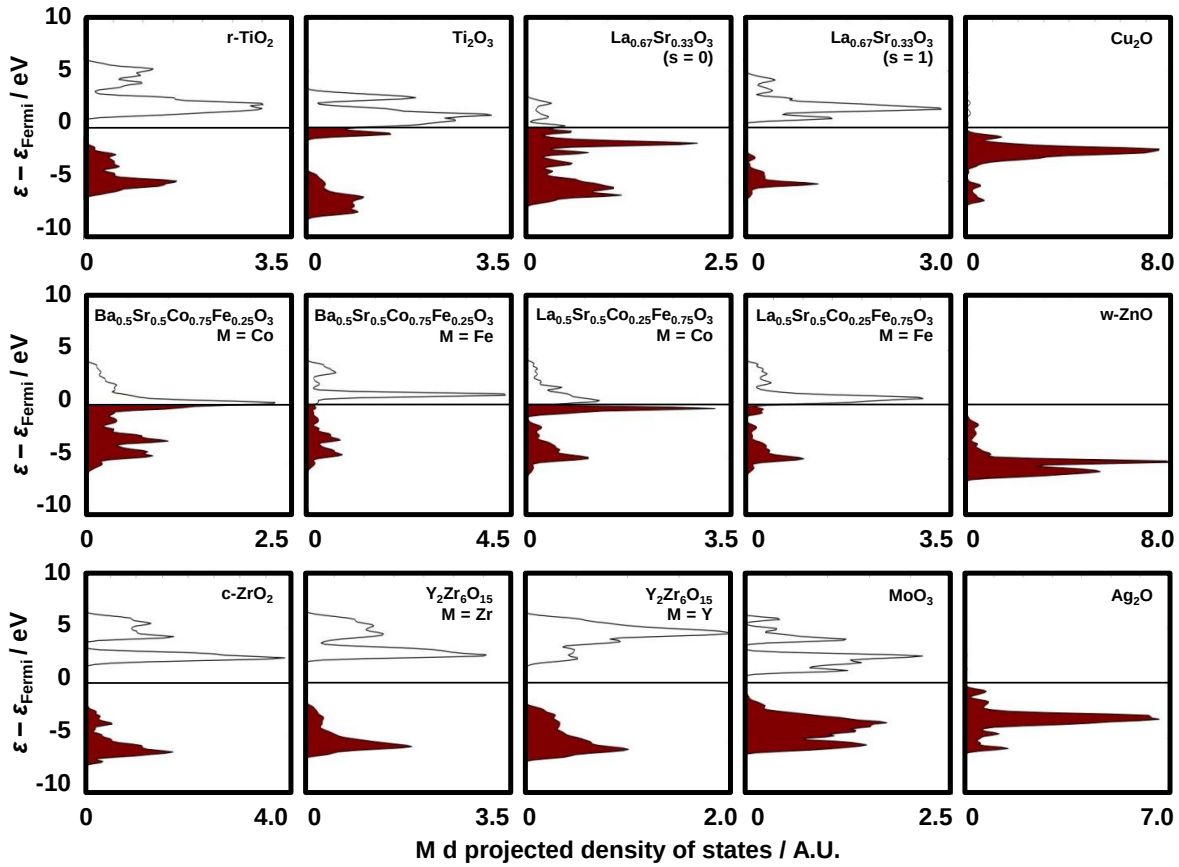

Figure S1: The metal (M) d projected density of states plots for the indicated bulk metal oxides (all calculations are with the Hubbard U = 0). The Fermi level is marked with a solid line and plots for both spins (s) are given for $La_{0.67}Sr0_{.33}O_3$ to show the correctly computed half-metallicity.

2.4. Oxygen-vacancy formation

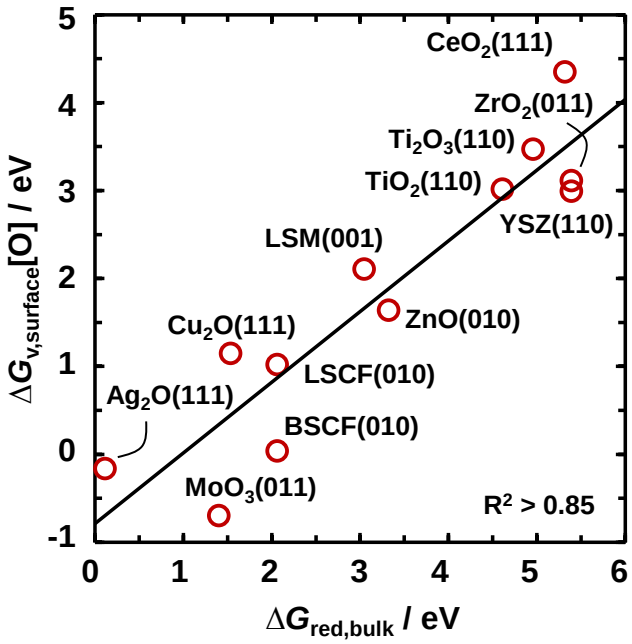

Figure S2: The DFT-calculated free energy of forming oxygen vacancies at a stable metal oxide surface *vs*. the free energy of reducing the bulk oxide at 25°C and 1 bar to the metal (except reduction of the highly oxidized MoO_3 to MoO_2). A solid line marks a linear regression: $\Delta G_{\mathrm{v,surface}}[\mathrm{O}] = 0.8041 \times \Delta G_{\mathrm{red,bulk}} - 0.7872$ eV.

We note, while the correlation of the free energy of forming oxygen vacancies at a metal oxide surface with the bulk-formation energy of a metal oxide (Figure 3) includes the discussed approximations for the bulk-formation energies of the mixed metal oxides:

$$\Delta G_{\mathrm{v,surface}}[\mathrm{O}] = -4.088 \times 10^{-3} \frac{\mathrm{eV} \times \mathrm{mol\ O_2}}{\mathrm{kJ}} G_{\mathrm{f,bulk}}^{25°\mathrm{C},1\ \mathrm{bar}} - 1.029\mathrm{eV} \qquad \text{(S4)}$$

excluding these approximations from the correlation:

$$\Delta G_{\mathrm{v,surface}}[\mathrm{O}] = -4.116 \times 10^{-3} \frac{\mathrm{eV} \times \mathrm{mol\ O_2}}{\mathrm{kJ}} G_{\mathrm{f,bulk,binary}}^{25°\mathrm{C},1\ \mathrm{bar}} - 0.9458\mathrm{eV} \qquad \text{(S5)}$$

yields a relative error of $100\% \times \left(G_{\mathrm{f,bulk}}^{25°\mathrm{C},1\ \mathrm{bar}} - G_{\mathrm{f,bulk,binary}}^{25°\mathrm{C},1\ \mathrm{bar}}\right) / G_{\mathrm{f,bulk}}^{25°\mathrm{C},1\ \mathrm{bar}} \approx 4.7\%$.

2.5. Oxygen-vacancy conduction

While Brønsted-Evans-Polanyi (BEP) relations have been employed to describe surface reactions at structurally similar metal oxide surfaces[13] we find that a simple BEP relation does not describe the oxygen conduction across structurally different metal oxide surfaces (Figure S3). The vacancy diffusion can be described thermodynamically by the energy difference between the free energy of forming the vacancy at the surface and in the subsurface,

such that $\delta G_{rxn} = \Delta G_{v,subsurface}[O] - \Delta G_{v,surface}[O]$ describes the conduction of vacancies from the surface into the subsurface (Figure S3A). This reaction is limited kinetically by an activation energy, $\delta G_{act} = \Delta G_{TS} - \Delta G_{v,surface}[O]$ that is determined by the free energy of the transition state.

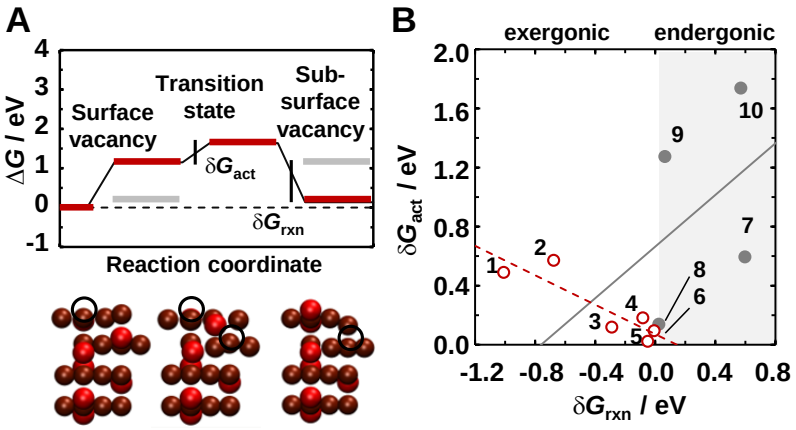

Figure S3: (A) Definition of the activation energy, δG_{act}, and the free energy of reaction, δG_{rxn}, for the vacancy diffusion shown schematically for $Cu_2O(111)$. Exergonic (endergonic) diffusion of oxygen vacancies (marked with black circles) from the surface into the subsurface is shown in red (gray). (B) Brønsted-Evans-Polanyi relations for an exergonic (red symbols) or endergonic (gray symbols) oxygen-vacancy diffusion. The numbered surfaces area: 1) $Cu_2O(111)$, 2) $Ag_2O(111)$, 3) $CeO_2(111)$, 4) BSCF(010), 5) $Ti_2O_3(110)$, 6) LSCF(010), 7) YSZ(110), 8) $ZrO_2(011)$, 9) $TiO_2(110)$, and 10) ZnO(010).

Opposite to the expected linear correlation, we find that for an exergonic diffusion process (*e.g.*, for Cu_2O) the activation energy scales linearly with the amount of energy that is liberated during the diffusion step, while for an endergonic diffusion process (*e.g.*, for ZnO) the activation energy scales linearly with the amount of energy that is absorbed during the vacancy diffusion. However, given the lack of self-similarity in the set of modeled metal oxide surfaces and the lack of monotony in the discussed endergonic and exergonic correlations, a definite conclusion on the use of simple BEP relations for the conduction of oxygen in metal oxides across the periodic table requires additional studies.

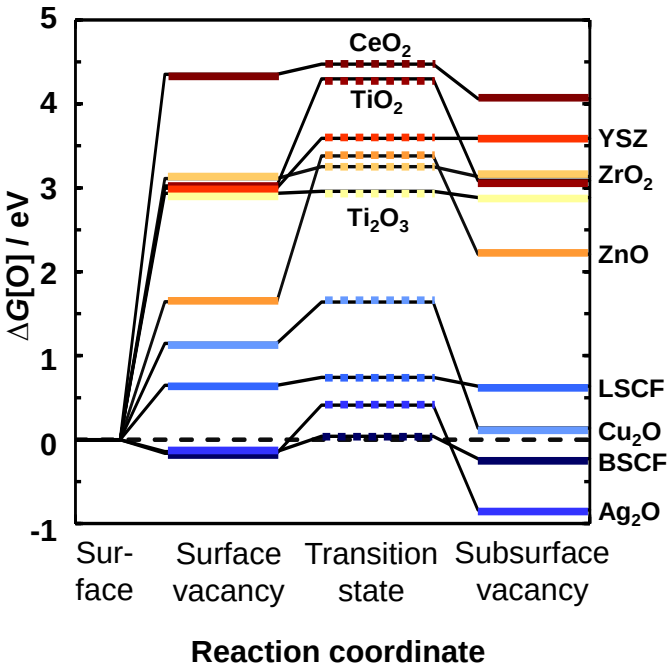

Figure S4: Free energy diagrams for the formation of an oxygen vacancy at the surface and the transition state for the diffusion of the surface vacancy to the thermodynamically most favorable subsurface position (where negative free energies indicate spontaneous processes, *i.e.*, below the dashed line). All energies are relative to the stoichiometric oxide surface and oxygen in the gas phase. The specific metal oxide surface is indicated with the metal oxide bulk stoichiometry. For clarity, the free energies values of the transition state are shown with dotted lines and are in eV: 0.04 (BSCF), 0.41 (Ag_2O), 0.74 (LSCF), 1.64 (Cu_2O), 2.96 (Ti_2O_3), 3.25 (ZrO_2), 3.38 (ZnO), 3.59 (YSZ), 4.30 (TiO_2), and 4.47 (CeO_2).

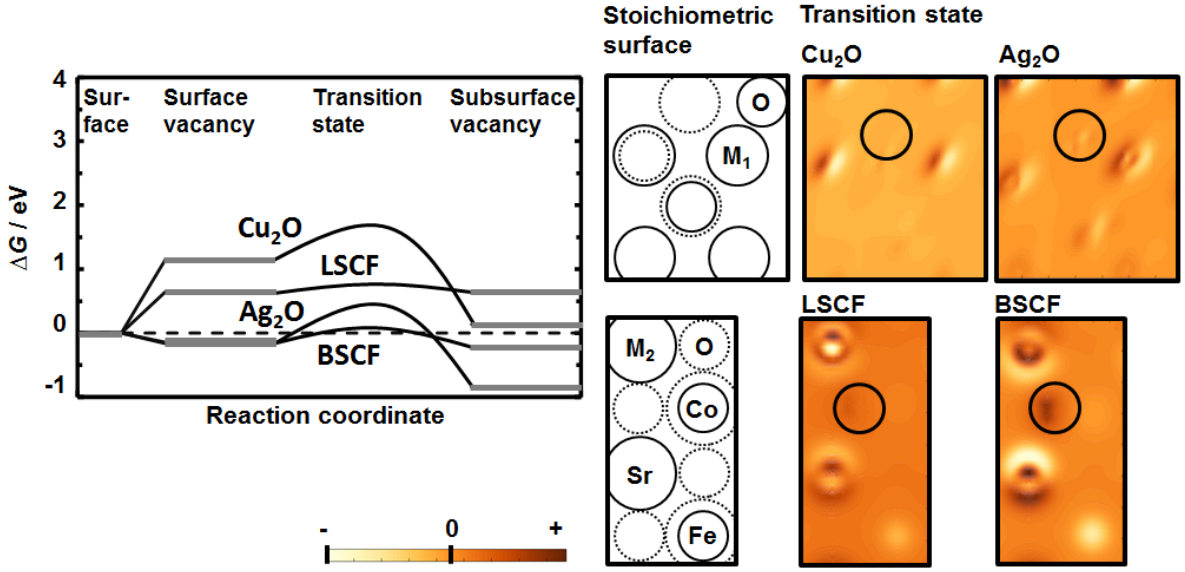

Figure S5: Free energy diagram for the oxygen-vacancy formation and diffusion for BSCF, Ag_2O, LSCF and Cu_2O respectively (detail from Figure 7; the metal oxide surfaces are indicated with the stoichiometric metal oxide composition). Negative free energies indicate spontaneous processes, *i.e.*, below the dashed line. All energies are relative to the stoichiometric surface and oxygen in the gas phase. The correlating charge density differences of the transition state are shown on the right (a schematic of the surface is given as reference, where M_1 = Ag or Cu and M_2 = La or Ba) in units of the elementary charge per $Å^3$ (shown qualitatively with a scale bar that indicates 0) at the height of the oxygen vacancy.

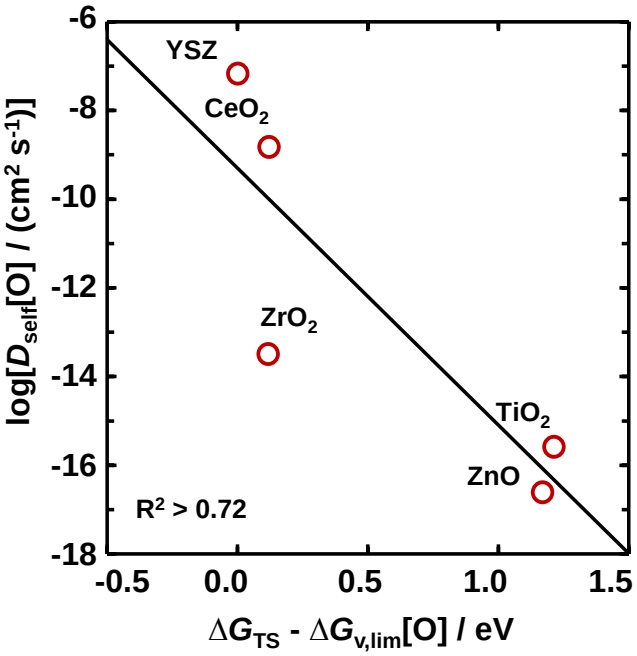

Figure S6: The average oxygen self-diffusion constant at 763 ± 39 °C (taken from the literature cited within the article, Figure 6) *vs.* the difference between the free energy of the transition state, ΔG_{TS}, and the limiting free energy of the oxygen-vacancy formation at the surface or subsurface, $\Delta G_{v,lim}[O]$ for metal oxides of the group with a thermodynamically highly endergonic diffusion path. $\Delta G_{v,lim}[O]$ is the energy value that is closer to the value of the transition state, such that the oxygen vacancies are assumed to diffuse into the direction that is favored thermodynamically, *i.e.*, away from the metal oxide surface if $\Delta G_{v,subsurface}[O] < \Delta G_{v,surface}[O]$ and $\Delta G_{v,lim}[O] = \Delta G_{v,surface}[O]$, and vice versa. The surface models are indicated with the stoichiometric metal oxide composition. The solid line is a linear regression.

3. References

[1] I. Barin, Thermochemical Data of Pure Substances **1993** (VCH Verlagsgesellschaft-mbH, 0–6940Weinheim, Federal Republic of Germany), ISBN 3–527–28531–8.

[2] P. S. Manning, J. D. Sirman, J. A. Kilner, *Solid State Ionics* **1997**, *93*, 125.

[3] Z. W. Cui, Y. Sun, J. M. Qu, *Solid State Ionics* **2012**, *226*, 24.

[4] U. Brossmann, R. Würschum, U. Södervall, H. E. Schaefer, *J. Appl. Phys.* **1999**, *85*, 7646.

[5] U. Brossmann, G. Knöner, H. E. Schaefer, R. Würschum, *Rev. Adv. Mater. Sci.* **2004**, *6*, 7.

[6] M. S. Khan, M. S. Islam, D. R. Bates, *J. Mater. Chem.* **1998**, *8*, 2299.

[7] M. J. Pietrowski, R. A. De Souza, M. Fartmann, R. ter Veen, M. Martin, *Fuel Cells* **2013**, *13*, 673.

[8] W. Eichenauer, G. Müller, *Z. Metallk.* **1962**, *53*, 321.

[9] T. A. Ramanarayanan, R. A. Rapp, *Metall. Trans.* **1972**, *3*, 3239.

[10] H. Rickert, R. Steiner, *Z. Phys. Chem.-Frankfurt* **1966**, *49*, 127.

[11] W. J. Moore, Y. Ebisuzaki, J. A. Sluss, *J. Phys. Chem.* **1958**, *62*, 1438.

[12] C. L. Muhich, B. W. Evanko, K. C. Weston, P. Lichty, X. H. Liang, J. Martinek, C. B. Musgrave, A. W. Weimer, *Science* **2013**, *341*, 540.

[13] A. Vojvodic, F. Calle-Vallejo, W. Guo, S. Wang, A. Toftelund, F. Studt, J. I. Martínez, J. Shen, I. C. Man, J. Rossmeisl, T. Bligaard, J. K. Nørskov, F. Abild-Pedersen, *J. Chem. Phys.* **2011**, *134*, 8.